



TECHNICAL ARTICLE

Different Effects of Body-Centered Cubic and Face-Centered Cubic Chromium Precipitations on Mechanical Properties and Wear Resistance of Cu-Cr-Zr Alloy

Dezhi Liu, Baoxu Huang , Changzheng Wang, Jie Ma, and Xingchuan Zhao

Submitted: 18 December 2021 / Revised: 22 April 2022 / Accepted: 6 May 2022 / Published online: 19 May 2022

Commercial high strength and high electrical conductivity Cu-0.67Cr-0.3Zr alloy was directionally solidified and subsequent aged. The specific strengthening mechanism of FCC and BCC structured chromium precipitations was discussed in detail. The strengthen effect of FCC Cr precipitation with a size less than 35 nm follows shear strengthening mechanism, while that of BCC Cr precipitation with size greater than 1.4 nm follows non-shear strengthening mechanism. After aging treatment, the yield strength of the alloy with a solidification rate of 50 $\mu\text{m/s}$ increases from about 140 to 205 MPa, which is due to the transformation of Cr precipitation from FCC to BCC. Besides, the matrix purification caused by phase transformation increases the electrical conductivity. In addition, the wear resistance of the alloy is also improved with the increase in strength. These excellent properties make the alloy have the potential to be competent as the high-speed railway contact lines.

Keywords conductivity, Cu-Cr-Zr alloy, mechanical property, precipitation, strengthening mechanism

1. Introduction

Cu-Cr-Zr alloy is widely used in electronic lead frames, resistance welding electrodes, high-speed railway contact lines, and other fields because of its high strength and high conductivity (Ref 1-4). Fu et al. reported that after rolling 95% at room temperature and aging at 723 K for 1 h, the tensile strength and electrical conductivity of Cu-0.98Cr-0.057Zr alloy reach 669 MPa and 74.5% IACS, respectively (Ref 5). Sun et al. obtained the Cu-1.0Cr-0.1Zr alloy with a tensile strength of 700 MPa and electrical conductivity of 78.5% IACS by dynamic plastic deformation at liquid nitrogen temperature (Ref 6). The high strength comes from the combination of fine precipitation strengthening, grain strengthening and deformation strengthening. However, the specific strengthening effect of precipitation in Cu-Cr-Zr alloy is not clear.

The strengthening effect of precipitation depends on its type, size, dispersion, and volume fraction (Ref 7, 8). In Cu-Cr alloys and modified Cu-Cr alloys, such as Cu-Cr-Zr and Cu-Cr-Fe alloys, face-centered cubic (FCC) and body-centered cubic (BCC) Cr precipitations were found. Although BCC Cr

precipitation is the equilibrium phase, the nucleation barrier of FCC Cr precipitation is low and can exist as metastable phase. Further research shows that FCC Cr precipitation is coherent with the matrix, while BCC Cr precipitation has a N-W or K-S orientation relationship with the matrix (Ref 9, 10).

Wang et al. reported that in their work involving Cu-0.43Cr-0.39Zr alloy, only FCC Cr precipitation is formed after aging at 723 K for 8 h. And the microhardness of 138 HV_{0.2} comes from the large amount of fine coherent FCC Cr precipitations (Ref 11). In addition, a large number of research results show that BCC Cr precipitation can be formed during aging process and has a strong strengthening effect (Ref 12, 13). The above results show that both FCC and BCC Cr precipitations have good strengthening effect on the matrix. In view of their different orientation relationship with the matrix, their strengthening mechanism should also be different. However, there are limited reports in this regard. On the other hand, the Cr concentration in the two precipitations is different. The Cr concentration in FCC Cr precipitation with a volume less than 20 nm³ is only about 50 at.%, whereas it is about 90 at.% in BCC Cr precipitation (Ref 9). Hence, FCC Cr precipitation inevitably accounts for a large volume fraction of the alloy and can thus adversely affect electrical conductivity.

Wang et al. observed that in as cast Cu-0.8Cr alloy, BCC Cr particles were formed as a network distribution in large grains (Ref 14). They explained that the formation of BCC Cr particles was due to the exceeded solubility limit (0.65 wt.%) at the eutectic temperature of 1349 K. According to the Cu-Cr binary phase diagram and solidification theory, these BCC Cr particles are the product of eutectic reaction. And the distribution and volume content of eutectic are greatly affected by the growth rate. Therefore, in the present work, the nominal Cu-0.67Cr-0.3Zr (wt.%) alloy was directionally solidified at different growth rates. The microstructure and mechanical

Dezhi Liu, Baoxu Huang, Changzheng Wang, Jie Ma, and Xingchuan Zhao, School of Materials Science and Engineering, Liaocheng University, Liaocheng 252000, China. Contact e-mail: huangbaoxu@lcu.edu.cn.

properties of the alloy before and after aging treatment were studied. And the effects of different types of Cr precipitation on the wear resistance were discussed.

2. Experimental Procedure

The alloy investigated in the present study is a commercial Cu-0.67Cr-0.3Zr alloy (wt.%). The specimen was enveloped in a high purity Al₂O₃ tube with an inner diameter of 8.5 mm and length of 80 mm. Directional solidification experiments were conducted in a Bridgman vertical vacuum furnace. The alloy was melted by a tungsten aluminum heater and then kept isothermal for 20 min to homogenize the origin composition. Subsequently, the specimen was moved downward at 50 and 200 μm/s, which is close to the actual casting. During the solidification process, the alloy melt was kept at 1893 K. The velocity of the downward movement was regarded as the growth rate along the axial direction (Ref 15). After directional solidification, all the specimens were isothermal aged at 723 K for 4 h.

Before the microstructure of the specimens was characterized by optical microscopy and Merlin Compact scanning electron microscopy (SEM) with energy-dispersive spectrometry (EDS) and electron backscattering diffraction (EBSD) detector, the specimens were ground on sandpaper and then polished by an electro-polishing instrument for 60 s at a voltage of 10 V using a mixture of 25% phosphoric acid, 25% alcohol, and 50% distilled water as the electrolyte. The cross section of the specimens was tested by D8 Advanced x-ray Diffraction (XRD) to qualitatively and quantitatively analyze the phase. Cu Kα radiation was used in the test, with a scanning range of 30° ~ 80° and a scanning rate of 3°/min. The precipitations were characterized by transmission electron microscopy (TEM; FEI Talos F200X) with EDS. The TEM samples were prepared using an automatic twin-jet electro-polisher at 243 K. The voltage was set to 15 V, and a mixture of 50% distilled water and 25% ethanol (95%) and 25% phosphoric acid (85%) was used as the electrolyte. The samples were then subjected to ion thinning.

Resistivity measurements were performed on the basis of a four-point method using an RTS-11 metal tester. The electrical resistivity acquired was compared with the standard specimen to get the electrical conductivity (%IACS, International Annealed Copper Standard). Tensile tests were performed at room temperature using Instron 5565 as per the guidelines of GB/T 22.1-2010, and the size of specimens is shown in Fig. 1. The Vickers microhardness of the specimens was measured

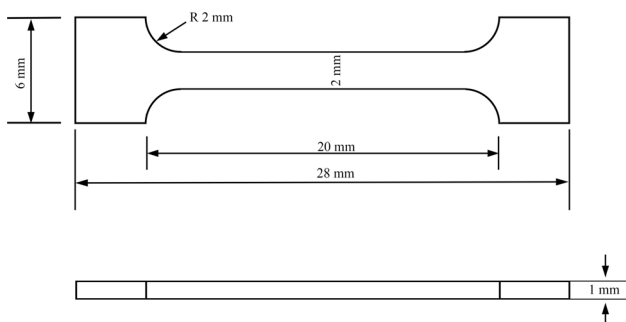


Fig. 1 The size of specimen for tensile testing

with a Buehler Micromet 2003 machine under 500 g load (4.9 N) for 10 s. The dry friction and wear test were carried out on the reciprocating friction and wear tester (MFT-EC4000) at room temperature (about 25 °C) in accordance with the ASTM G133-05 standard (Ref 16). GCr15 ball with a diameter of 6mm was selected as the friction pair according to the specimen size. The loading force is 5N, and the reciprocating frequency is 2Hz. The amplitude of each experiment was 5 mm for 30min. The data were presented as the average of at least three measurements. Before the electrical conductivity, mechanical properties and wear resistance tests, the surface of the specimens was polished to ensure the accuracy of the test results.

After friction tests, the wear surface was characterized and analyzed by SEM and EDS. In addition, the wear rate was calculated by the following equation (Ref 17, 18)

$$\text{Wear rate mm}^3/(\text{N} \cdot \text{mm}) = \text{Wear Volume}/\text{Frictional work}$$

where the wear volume is the product of the cross-sectional area of the groove and the length of the wear track, the frictional work is the product of the load and the sliding distance.

3. Results and Discussion

3.1 Characterization of Microstructure

3.1.1 Microscopy. Figure 2 shows the optical microstructures of the cross section and longitudinal section of the as cast specimens. The structure of the cross section is equiaxed, while that of the longitudinal section is striped. At a higher growth rate of 200 μm/s, the equiaxed structure is smaller and the strip is thinner. In order to determine whether the equiaxed structure is columnar or cellular, EBSD was carried out, and the results are shown in Fig. 3. Dozens of equiaxed structures have similar crystal orientation. The analysis results based on Euler angle demonstrate that the spatial orientation difference of adjacent equiaxed structures is about 0.3 degrees, which indicates that the equiaxed structures are cellular crystals rather than columnar. At both growth rates, the grain size of the specimens is larger than a few hundred microns. According to the theory that cellular crystals are formed under relatively small supercooling (Ref 19) and the fact that crystals grow under a positive temperature gradient, constitutional supercooling occurs during crystal growth.

Besides, a large number of rod-like second phase were detected at the cell boundaries, but not in the cell at both solidification rates, as shown in Fig. 2 and 4(a) and (b). According to the cellular growth theory (Ref 20), eutectic is generally formed at the junctions with two or more cells. Considering that the original composition is close to the hypoeutectic composition of Cu Cr binary alloy, it can be inferred that the rod-like second phase and the surrounding phase are eutectic reaction products. Because the volume of the two phases in eutectic structure varies greatly, the phase with less volume fraction tends to present rod-like morphology (Ref 21). It is noteworthy that the eutectic structure in the specimen grown at 200 μm/s is finer than that grown at 50 μm/s, as shown in Fig. 2. According to the solidification theory, the inter fiber spacing λ between rods is related to the solidification rate R (Ref 20).

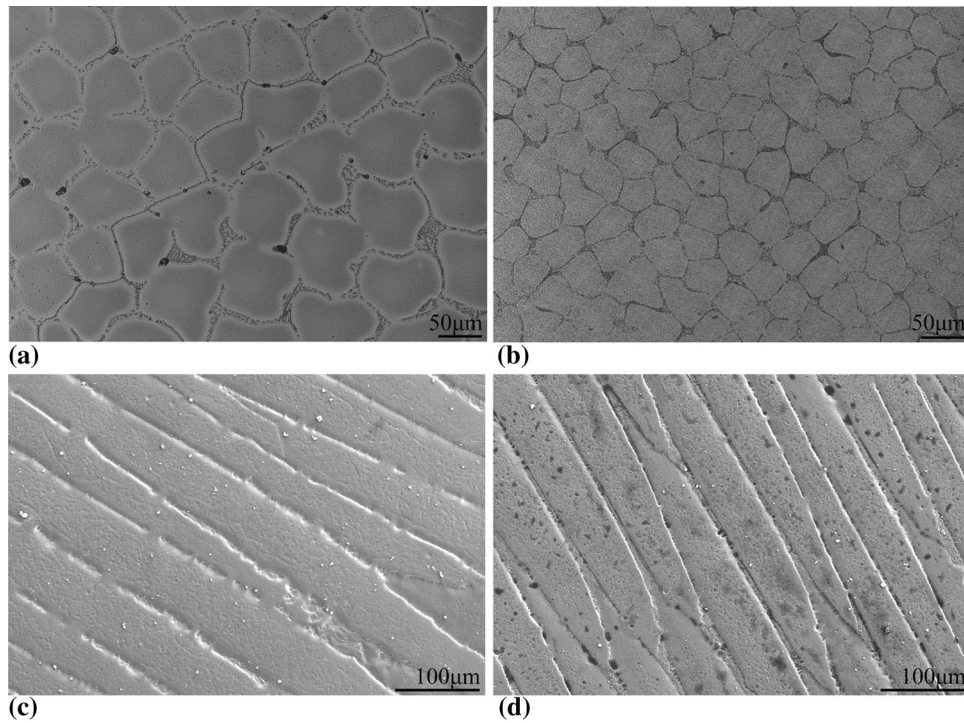


Fig. 2 Optical images of the cross section (a, b) and SEM images of the longitudinal section (c, d) of the specimens at growth rates of 50 $\mu\text{m/s}$ (a, c) and 200 $\mu\text{m/s}$ (b, d)

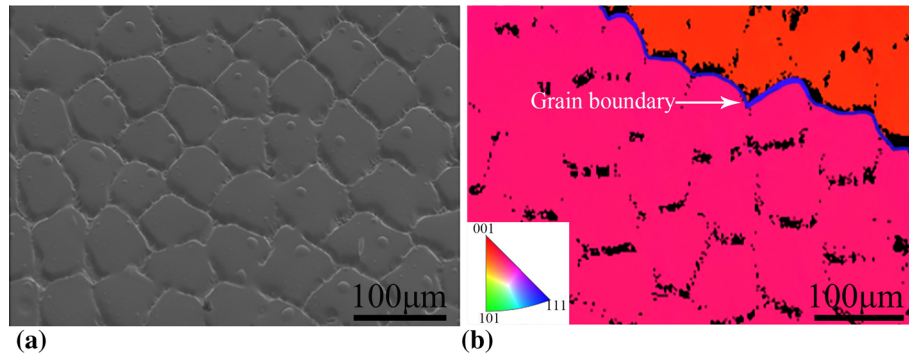


Fig. 3 EBSD result of the cross section of the specimen at a growth rate of 50 $\mu\text{m/s}$ (a) SEM image and (b) color coded grain orientation distribution map inserted with Inverse Pole Figure Z (normal to cross section)

$$\lambda^2 R = \text{constant} \quad (\text{Eq 1})$$

From Eq 1, it can be clearly seen that λ decreases with the increase in growth rate.

The results of the selected area diffraction pattern (SADP) and EDS of TEM confirm that the rod-like phase in eutectic is BCC Cr phase and that the Cr content is about 93 wt.% (Fig. 5a, b, and c). Further analysis of SADP showed that $(0\bar{1}1)_{Cr} // (\bar{1}11)_{Cu}$ and $[\bar{1}11]_{Cr} // [0\bar{1}1]_{Cu}$, i.e., the K-S orientation relationship between the BCC Cr phase and Cu phase. Besides, uniformly distributed nanoprecipitations were also found in cells (Fig. 5d). These nanoprecipitations have an FCC crystal structure and are coherent with the Cu matrix, which is consistent with the results of A. Chbihi (Ref 9) and Yue Liu (Ref 7). For the nano-FCC Cr precipitation in Cu-Cr alloy, Chbihi et al. proved that the concentration of Cr increases with an increase in precipitation size. With the increase in precipi-

tation size from 20 to 80 nm³, Cr content increases from about 50 at.% to about 90 at.% (Ref 9). TEM observation shows that the average radius of these FCC precipitations is about 2 nm, indicating that the Cr content is around 80 at.%.

After aging treatment, the eutectic structure is retained and a large number of precipitations with the size of hundred nanometers were found in cells, as shown in Fig. 4(c), (d). These precipitations were characterized by TEM, as shown in Fig. 6(a). The analysis results of SADP confirm that these precipitations are BCC Cr phase. Besides, uniformly distributed precipitations ranging in size from several nanometers to hundreds of nanometers were also found, as shown in Fig. 6(a), (c). For these nanoscale precipitations, it is difficult to detect their diffraction spots by electron diffraction due to their small size. However, high-resolution transmission electron microscopy (HRTEM) showed that these nanoprecipitations are BCC Cr phase incoherent with the matrix, as shown in Fig. 6(d). In

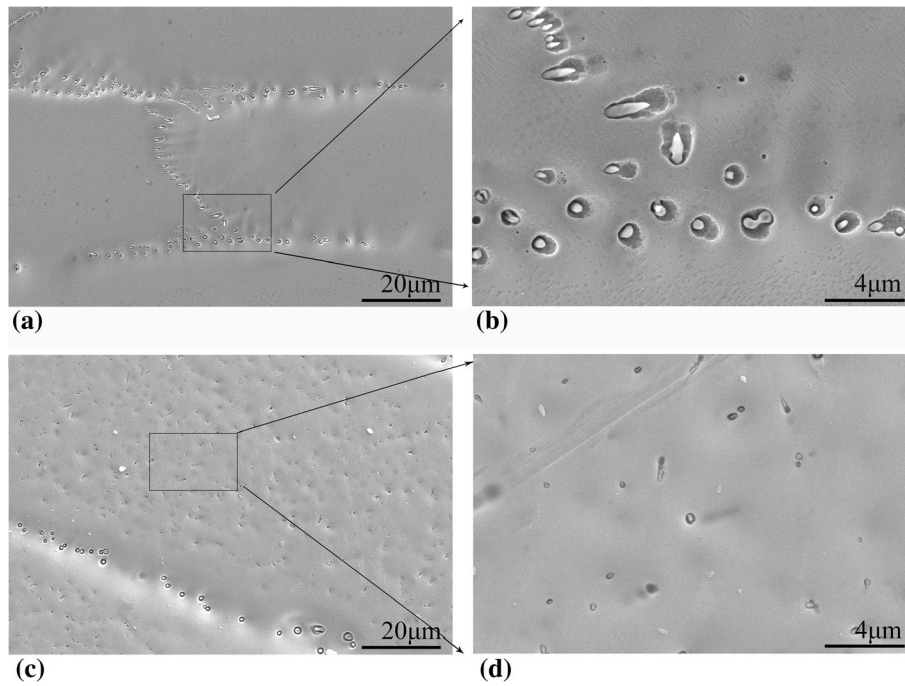


Fig. 4 SEM images of cross section before (a, b) and after aging treatment (c, d) at the growth rate of 50 $\mu\text{m/s}$ (a, c) and 200 $\mu\text{m/s}$ (b, d)

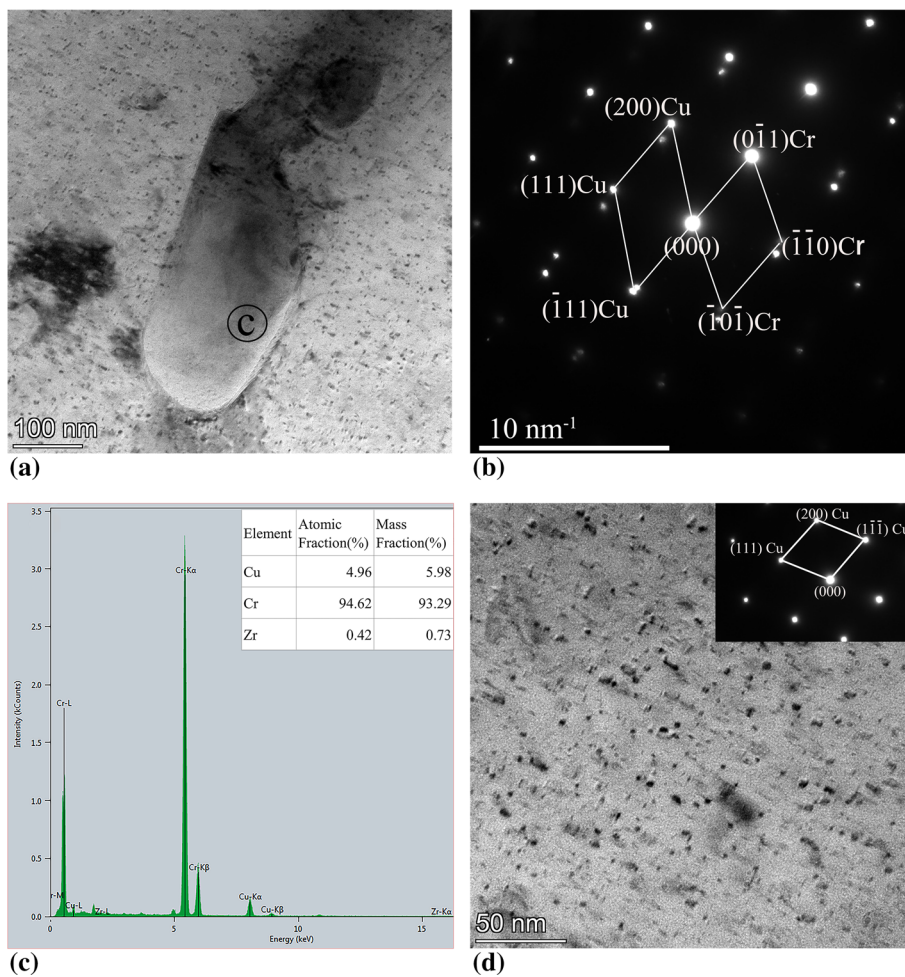


Fig. 5 TEM image (a), electron diffraction pattern (b), and EDX result of the precipitation (c) and TEM image of the matrix (d) of the as cast specimen at a growth rate of 50 $\mu\text{m/s}$

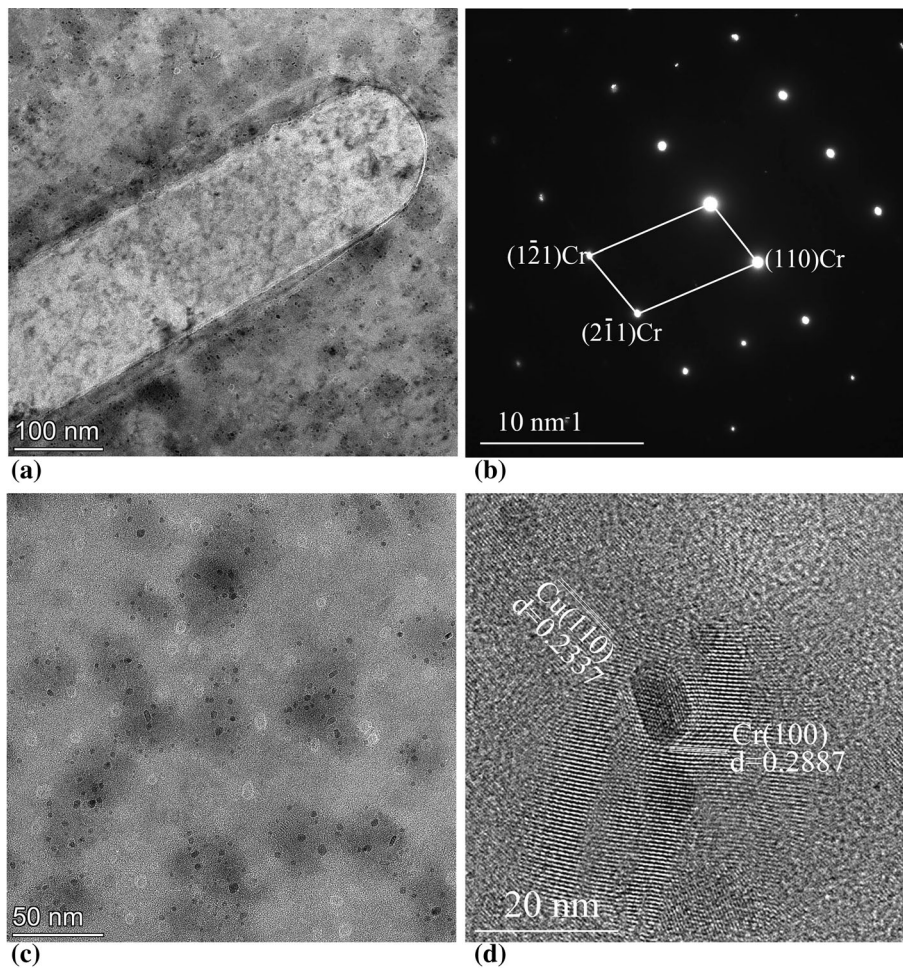


Fig. 6 TEM image (a), electron diffraction pattern (b) of the BCC Cr precipitate and TEM (c), HRTEM images (d) of nano-Cr precipitates in the aged specimen at growth rate of 200 $\mu\text{m/s}$

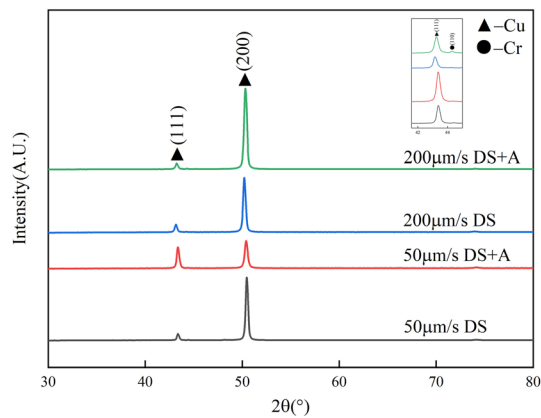


Fig. 7 XRD patterns of the specimen before and after aging treatment

addition, it is important to note that FCC Cr precipitations disappear, which indicates that all FCC Cr precipitations were transformed into stable BCC Cr precipitations during aging process. However, the size of BCC Cr precipitation increased and the density decreased compared to that of FCC Cr precipitation.

3.1.2 X-Ray Diffraction. Figure 7 shows the XRD patterns of the specimens before and after aging treatment. For as cast specimens, only FCC Cu phase was detected and showed strong [001] growth texture. After aging treatment, a weak Cr (110) diffraction peak appeared, indicating the formation of BCC Cr precipitation. The lattice parameters of Cu matrix are calculated and listed in Table 1. It can be clearly seen that the lattice parameter is closer to that of pure Cu (0.36147 nm (Ref 22)) after aging treatment, indicating that the matrix has been purified.

4. Mechanical Properties and Strengthening Mechanism

4.1 Mechanical Properties

The mechanical properties of the specimen studied under different conditions are listed in Table 2. It can be clearly seen that both of the strength and hardness were greatly improved after aging treatment. The microstructure characterization results show that the only change after aging treatment is that FCC Cr precipitation is replaced by BCC Cr precipitation. Therefore, it can be inferred that the increase in strength and

Table 1 lattice parameter of the specimen before and after aging treatment

	As cast		After aging treatment	
	50, $\mu\text{m/s}$	200, $\mu\text{m/s}$	50, $\mu\text{m/s}$	200, $\mu\text{m/s}$
Lattice parameter, nm	0.36204	0.36214	0.36165	0.36171

Table 2 Mechanical properties and electrical conductivity of the Cu-0.67Cr-0.3Zr alloy under different conditions

Growth rates	As cast		After aging treatment	
	50, $\mu\text{m/s}$	200, $\mu\text{m/s}$	50, $\mu\text{m/s}$	200, $\mu\text{m/s}$
Yield strength, $\sigma_{0.2}$ MPa	140.8 \pm 2.5	143.5 \pm 3.0	205.1 \pm 5.0	207.7 \pm 5.2
Tensile strength, MPa	205.7 \pm 11.3	215.6 \pm 10.9	280.4 \pm 16.2	270.5 \pm 25.3
Elongation, %	25.3 \pm 3.5	21.5 \pm 3.2	25.5 \pm 3.0	26.0 \pm 4.3
Vickers hardness, HV	49.6 \pm 2.6	70.08 \pm 1.6	74.26 \pm 3.74	84.08 \pm 3.58
Electrical conductivity, %IACS	46.61 \pm 1.54	45.24 \pm 1.14	76.26 \pm 2.52	78.85 \pm 4.08

hardness is the result of transformation of precipitation from FCC to BCC.

4.2 Strengthening Mechanism

For eutectic structure, the yield strength follows a relationship similar to the Hall-Petch relationship used for grain boundary strengthening (Ref 23).

$$\sigma = \sigma_0 + k\lambda^{-1/2} \quad (\text{Eq 2})$$

Here σ_0 is a friction stress, k is a material constant. The microstructure characterization shows that the fiber spacing λ of eutectic in the specimen grown at 200 $\mu\text{m/s}$ is less than that grown at 50 $\mu\text{m/s}$. The mechanical properties of as cast specimen verify that the yield strength increases with the increase in growth rate, i.e., the decrease in fiber spacing λ .

For the coherent precipitate, the critical particle size d_c for the dislocation shearing to looping transition can be estimated by the following equation (Ref 24, 25):

$$d_c = \frac{Gb^2}{\gamma} \quad (\text{Eq 3})$$

where G is the shear modulus of the matrix, b is the Burgers vector of a matrix dislocation, γ is the sum of the anti-phase boundary energy and the interfacial energy of the new interface created by the cutting. In the case of coherent FCC Cr precipitation, the anti-phase boundary energy is zero because ordered phase does not form during precipitation. And the interfacial energy between the coherent Cr precipitation and the matrix is 86 mJ m^{-2} (Ref 9). Based on the data in Table 3, the critical particle size can be calculated to be 35 nm. TEM observation showed that the size of FCC precipitation is less than 5 nm, so it can be sheared during deformation. Thus, the strength effect of FCC Cr precipitation follows the shearing mechanism. It is known that three main factors associated with shearing mechanism: the coherence effect, the modulus effect, and the chemical effect (Ref 26-28). The chemical effect is not important in this case because an anti-phase boundary does not

form during the shearing. The coherence effect can be evaluated as (Ref 27)

$$\tau_{\text{Coh}} = k \left(\frac{G^3 b \varepsilon^3 r^3}{L_s^2 T(\theta)} \right)^{0.5} \quad (\text{Eq 4})$$

with

$$\varepsilon = \frac{1}{3} \left(\frac{1+\nu}{1-\nu} \right) \frac{\Delta a}{a} \quad (\text{Eq 5})$$

and

$$T(\theta) = \frac{Gb^2}{4\pi} \left(\frac{1+\nu-3\sin^2\theta}{1-\nu} \right) \ln \left(\frac{r_0}{r_i} \right) \quad (\text{Eq 6})$$

where k is a constant equal to 4.11 and 1.38 for edge and screw dislocation, respectively. Here, r is the mean radius and L_s is the surface to surface distance between two precipitations. In Eq 5 and 6, ν is Poisson's ratio, ε is the constrained strain produced by the stress free strain of linear lattice misfit δ , a is the lattice parameter of the matrix, Δa is the difference between lattice parameters of matrix and precipitation, the value of $\Delta a/a$ is 1.9% (Ref 29), r_0 is the distance between two precipitations along the dislocation line, which is equal to L_s due to the small size of FCC Cr precipitations, r_i is the dislocation core radius with values between b and $4b$ and θ is the angle between the dislocation line and its Burgers vector. For low energy screw dislocation, the value of coherency strengthening of $\tau_{\text{coh}}=33.1$ MPa is obtained for the present specimen.

The modulus effect is represented as (Ref 29):

$$\tau_{\text{mod}} = \frac{2T(\theta)}{bL_s} \left[\frac{\omega_1 |G_{\text{Cr}} - G_{\text{Cu}}| b^2 (\pi r/4b)^{\omega_2}}{2T(\theta)} \right]^{3/2} \quad (\text{Eq 7})$$

where ω_1 and ω_2 are two constants equal to 0.05 and 0.85, respectively. And the value of modulus strengthening of 121 MPa is obtained. To calculate the overall precipitation shear strengthening effect, the different mechanisms are superimposed according to:

Table 3 Parameters of the studied Cu-0.67Cr-0.3Zr alloy

Parameter	G _{Cu} , GPa	G _{Cr} , GPa	b, nm	ν	r, nm	L _s , nm	Strengthening effect, MPa
FCC Precipitates	45.5[7, 25]	...	0.256[7, 27]	0.34[7, 27]	2	20	125.4
BCC Precipitates
Minimum size	...	104.4[28]	3	30	524.3
BCC Precipitates
Maximum size	...	104.4[28]	150	1500	28.9

$$\tau_{\text{shear}} = \left(\frac{f_{\text{shear}}}{f_{\text{total}}} \right)^{0.5} \sqrt{\tau_{\text{coh}}^2 + \tau_{\text{mod}}^2} \quad (\text{Eq 8})$$

where f_{shear} is the fraction of coherent precipitation and f_{total} is the total fraction of precipitation. Here, $f_{\text{shear}}/f_{\text{total}}$ was assumed to be 1 in the present calculation due to the large number and small size of coherent FCC Cr precipitations. And the τ_{shear} value was calculated to be about 125.4 MPa. Therefore, the yield strength of the specimen should be about 177.4 MPa (shearing effect 125.4 MPa plus intrinsic lattice stress 52 MPa (Ref 30)), which is higher than the result of experiments (around 140 MPa). This difference can be attributed to the existence of eutectic. The fact that the experimental value of yield strength is lower than the theoretical value shows that the strengthening effect of eutectic structure is lower than that of FCC Cr precipitation.

Unlike FCC Cr precipitation, BCC Cr precipitation has a K-S orientation relative to the matrix. For the incoherent precipitation, the critical diameter d_c can be calculated by the following equation (Ref 24, 25):

$$d_c = \frac{4\pi G_m b}{G_p} \quad (\text{Eq 9})$$

where G_m and G_p are the shear modulus of the matrix and the precipitation, respectively. Based on the values presented in Table 3, a critical diameter of 1.4 nm was calculated. The minimum size of BCC Cr precipitations observed by TEM is 3 nm, so it will not be sheared during deformation. Therefore, the strengthening mechanism of BCC Cr precipitation follows the non-shearing mechanism and the Orowan equation (Ref 27, 28).

$$\sigma_{\text{Orowan}} = \frac{M G b}{2\pi\sqrt{1-\nu}} \cdot \frac{1}{L_s} \ln\left(\frac{\pi r}{2r_i}\right) \quad (\text{Eq 10})$$

where M is the average value for converting shear stress to tensile stress, and the value is 3.1. Based on the size of BCC Cr precipitation in cell ranging from a few nanometers to hundreds of nanometers, the strengthening effects of precipitation with maximum and minimum sizes are calculated. And the results are listed in Table 3. Compared with FCC Cr precipitation, the strengthening effect of BCC Cr precipitation with hundreds nanometers is weak, while that with a few nanometers is strong. And the coexistence of BCC Cr precipitations with different sizes and eutectic increases the actual yield strength to about 205 MPa.

From Table 2, it can be found that the yield strength increases with the increase in solidification rate, while the change in tensile strength seems to be independent of solidification rate. From the previous EBSD analysis results,

it can be seen that the grain size is large enough, so the effect of grain boundary strengthening can be ignored. Thus, based on microstructure observation, the main strengthening effect comes from eutectic and precipitation in the matrix. As per the Orowan strengthening mechanism, eutectic has little contribution to strengthening due to its large eutectic fiber spacing. Nevertheless, the decrease in eutectic fiber spacing with the increase in solidification rate can improve the yield strength. And this is reflected in the mechanical behavior of as cast specimens. Besides, it is worth noting that after aging treatment, the tensile strength decreases slightly with the increase in solidification rate. This may be due to the refinement of eutectic network, which greatly increases the interface area between eutectic and matrix. As a result, the volume content of BCC precipitation free zone is increased due to the growth of BCC Cr phase in eutectic during aging process (Ref 31). The increase in precipitation free zone reduces the amount of BCC Cr precipitation and weakens the effect of precipitation strengthening. The above discussion shows that the effect of eutectic structure change on strength has two aspects.

5. Wear Resistance

Figure 8 shows the SEM images and EDS mapping analysis of the wear tracks and adjacent substrates. The results of EDS mapping analysis show that oxygen exists in all wear tracks rather than adjacent substrates, which confirms the existence of oxidative wear mechanism.

Figure 9 shows the microstructure of wear surfaces of the specimen under different conditions. Due to the low strength of Cu matrix, plastic deformation occurs on all worn surfaces. Besides, it can be clearly seen that part of the worn surfaces are covered with a smooth and deformed tribolayer, which is formed by the mechanically mixing of wear debris. The results of EDS analysis, as shown in Fig. 8, indicate that these wear debris are oxidized. In addition, some shallow delamination craters exist on the worn surface of the specimens. Therefore, it can be deduced that the wear mechanisms are abrasive wear, oxidation wear and delamination. It is worth noting that the proportion of tribolayer of aged specimens increases. As a kind of wear resistance bearing layer, tribolayer will help to improve the wear resistance (Ref 32). The wear rate results calculated and listed in Table 4 show that the wear resistance is improved after aging treatment. Combined with the change in microstructure, it can be concluded that the wear resistance of the alloy is improved after Cr precipitation changes from FCC to BCC.

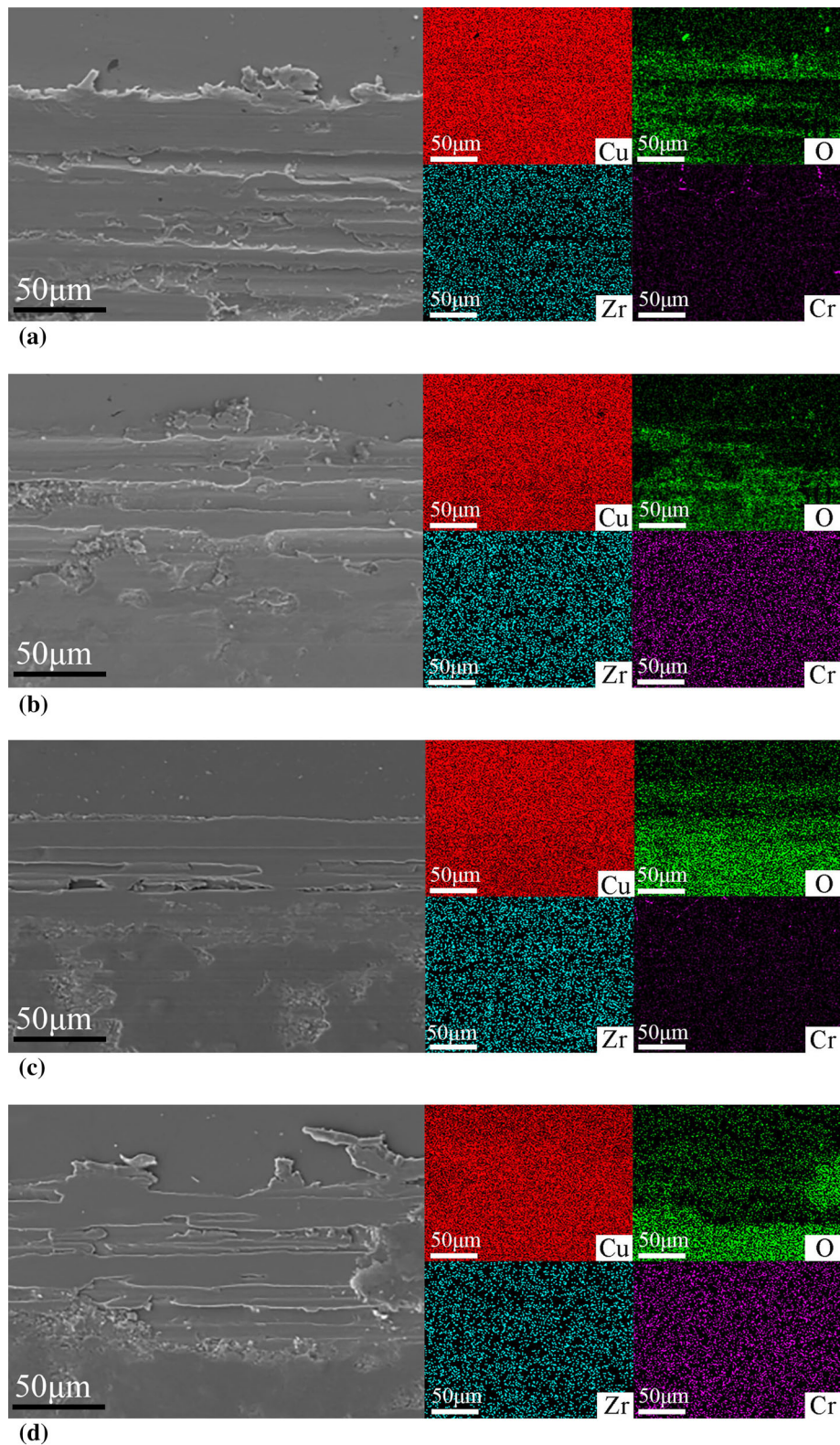


Fig. 8 SEM images and EDS mapping of the wear tracks of as cast specimen at the growth rate of 50 $\mu\text{m/s}$ (a), 200 $\mu\text{m/s}$ (b) and SA heat treated specimen at the growth rate of 50 $\mu\text{m/s}$ (c), 200 $\mu\text{m/s}$ (d)

6. Electrical Conductivity

As the scattering points of conducting electrons, the volume fraction of precipitation exerts a great influence on electron

resistivity (Ref 33, 34). Because BCC Cr precipitation (94.4 at.%) contains more solute Cr than FCC Cr precipitation (80 at.%), replacing FCC Cr precipitation with BCC Cr precipitation will promote the segregation of Cr and reduce the volume

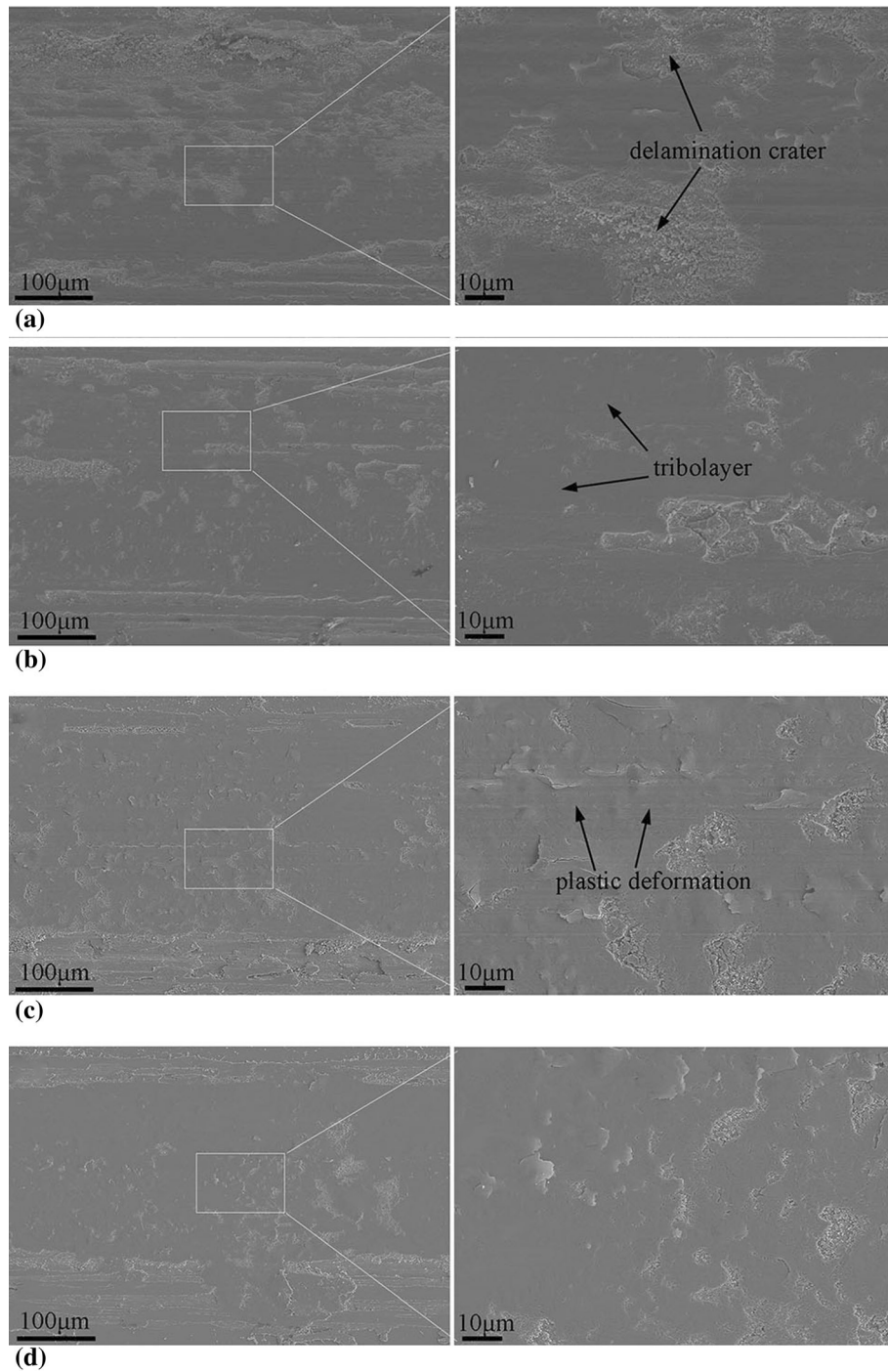


Fig. 9 SEM images of the wear track of as cast specimen at the growth rate of 50 $\mu\text{m/s}$ (a), 200 $\mu\text{m/s}$ (b) and SA heat treated specimen at the growth rate of 50 $\mu\text{m/s}$ (c), 200 $\mu\text{m/s}$ (d)

Table 4 Wear rate of specimen under different states

Growth rates	As cast		After SA	
	50, $\mu\text{m/s}$	200, $\mu\text{m/s}$	50, $\mu\text{m/s}$	200, $\mu\text{m/s}$
Wear rate, $\text{mm}^3/(\text{N}\cdot\text{m})$	3.04996×10^{-5}	0.48605×10^{-5}	0.388×10^{-5}	0.222×10^{-5}

fraction of precipitation. And XRD results confirmed the purification of matrix after aging treatment. As a result, the electrical conductivity is improved, as shown in Table 2.

7. Conclusion

In the present investigation, high strength and high conductivity Cu-0.67Cr-0.3Zr alloy was directionally solidified at the rate of 50 and 200 $\mu\text{m/s}$, respectively. The effects of solidification rate and precipitation transition from FCC to BCC on strength, microhardness, electrical conductivity and wear resistance of the alloy were studied. And the following conclusions can be drawn:

- (1) In the range of solidification rate from 50 to 200 $\mu\text{m/s}$, the alloy grows as cellular crystals. Eutectic is formed at the cell boundaries while nanometer FCC Cr precipitation uniformly distribute in the cell.
- (2) The eutectic fiber and eutectic network are obviously refined with the increase in solidification rate. The refinement of eutectic itself improves the yield strength. However, the refinement of eutectic network increases the BCC Cr precipitation free zone, which reduces the amount of precipitation and is harmful to the strength.
- (3) The strength effect of the coherent FCC Cr precipitation with size less than 35 nm follows shear strengthening mechanism, while that of BCC Cr precipitation with size greater than 1.4 nm follows non-shear strengthening mechanism.
- (4) Theoretical calculation shows that FCC Cr precipitation with a radius size of 2 nm and a separation distance of 20 nm only increased the yield strength by 125.4 MPa. In contrast, BCC Cr precipitation with a radius size of 3 nm and a separation distance of 30 nm can increase the yield strength by 524.3 MPa. This indicates that phase transformation of Cr precipitation plays an important role in improving the strength of the alloy.
- (5) With the increase in strength and hardness, via aging treatment, the wear rate decreases. And the main wear mechanisms are abrasive wear, oxidation wear and delamination.

Acknowledgments

This work was supported by the key projects of Liaocheng University (Grant No. 13KZ1201).

Reference

1. I.S. Batra, G.K. Dey, U.D. Kulkarni and S. Banerjee, Precipitation in a Cu-Cr-Zr Alloy, *Mater. Sci. Eng. A*, 2003, **356**, p 32–36. [https://doi.org/10.1016/S0921-5093\(02\)00852-3](https://doi.org/10.1016/S0921-5093(02)00852-3)
2. J.M. Zhou, D.G. Zhu, L.T. Tang, X.S. Jiang, S. Chen, X. Peng and C.F. Hu, Microstructure and Properties of Powder Metallurgy Cu-1%Cr-0.65%Zr Alloy Prepared by hot Pressing, *Vacuum*, 2016, **131**, p 156–163. <https://doi.org/10.1016/j.vacuum.2016.06.008>
3. Y. Pang, C.D. Xia, M.P. Wang, Z. Li, Z. Xiao, H.G. Wei, X.F. Sheng, Y.L. Jia and C. Chen, Effects of Zr and (Ni, Si) Additions on Properties and Microstructure of Cu-Cr Alloy, *J. Alloy. Compd.*, 2014, **582**, p 786–792. <https://doi.org/10.1016/j.jallcom.2013.08.146>
4. M. Hatakeyama, T. Toyama, J. Yang, Y. Nagai, M. Hasegawa, T. Ohkubo, M. Eldrup and B.N. Singh, 3D-AP and Positron Annihilation Study of Precipitation Behavior in Cu-Cr-Zr Alloy, *J. Nucl. Mater.*, 2009, **386–388**, p 852–855. <https://doi.org/10.1016/j.jnucmat.2008.12.266>
5. H. Fu, S. Xu, W. Li, J. Xie, H. Zhao and Z. Pan, Effect of Rolling and Aging Processes on Microstructure and Properties of Cu-Cr-Zr Alloy, *Mater. Sci. Eng., A*, 2017, **700**, p 107–115. <https://doi.org/10.1016/j.msea.2017.05.114>
6. L.X. Sun, N.R. Tao and K. Lu, A High Strength and High Electrical Conductivity Bulk CuCrZr Alloy with Nanotwins, *Scripta Mater.*, 2015, **99**, p 73–76. <https://doi.org/10.1016/j.scriptamat.2014.11.032>
7. Y. Liu, Z. Li, Y. Jiang, Y. Zhang, Z. Zhou and Q. Lei, The Microstructure Evolution and Properties of a Cu-Cr-Ag Alloy during Thermal-Mechanical Treatment, *J. Mater. Res.*, 2017, **32**(7), p 1324–1332. <https://doi.org/10.1557/jmr.2017.17>
8. Y.J. Zhou, K.X. Song, J.D. Xing et al., Precipitation Behavior and Properties of Aged Cu-0.23Be-0.84Co Alloy, *J. Alloys Compd.*, 2016, **658**, p 920–930. <https://doi.org/10.1016/j.jallcom.2015.10.290>
9. A. Chbihi, X. Sauvage and D. Blavette, Atomic Scale Investigation of Cr Precipitation in Copper, *Acta Mater.*, 2012, **60**, p 4575–4585. <https://doi.org/10.1016/j.actamat.2012.01.038>
10. Muzhi Ma, Zhou Li, Zhu Xiao, Hanrui Zhu, Xi. Zhang and Fenyang Zhao, Microstructure and Properties of a novel Cu-Cr-Yb Alloy with High Strength, High Electrical Conductivity and Good Softening Resistance, *Mater. Sci. Eng. A*, 2020, **795**, p 140001. <https://doi.org/10.1016/j.msea.2020.140001>
11. H. Wang, L. Gong, J. Liao, H. Chen, W. Xie and B. Yang, Retaining Meta-stable fcc-Cr Phase by Restraining Nucleation of Equilibrium bcc-Cr Phase in CuCrZrTi Alloys during Ageing, *J. Alloy. Compd.*, 2018, **749**, p 140–145. <https://doi.org/10.1016/j.jallcom.2018.03.238>
12. Fu. Huadong, Xu. Sheng, W. Li, J. Xie, H. Zhao and Z. Pan, Effect of Rolling and Aging Processes on Microstructure and Properties of Cu-Cr-Zr Alloy, *Mater. Sci. Eng. A*, 2017, **700**, p 107–115. <https://doi.org/10.1016/j.msea.2017.05.114>
13. G.Y. Li, S.Y. Li, L. Li, D.T. Zhang, J.D. Wang and Y.X. Tong, A High Strength and High Electrical Conductivity CuCrZr Alloy Prepared by Aging and Subsequent Cryorolling, *Vacuum*, 2021, **190**, p 110315. <https://doi.org/10.1016/j.vacuum.2021.110315>
14. Y. Wang, F. Huadong, J. Wang, H. Zhang, W. Li and J. Xie, Enhanced Combination Properties of Cu-0.8Cr Alloy by Fe and P Additions, *J. Nucl. Mater.*, 2019, **526**, p 151753. <https://doi.org/10.1016/j.jnucmat.2019.151753>
15. Ka. Gao, S. Li, Xu. Lei and Fu. Hengzhi, Effect of Solidification Rate on Microstructures and Orientations of Al-Cu Hypereutectic Alloy in Thin Crucible, *Cryst. Res. Technol.*, 2014, **49**, p 164–170. <https://doi.org/10.1002/crat.201300368>
16. ASTM International, Standard Test Method for Linearly Reciprocating Ball-on-Flat Sliding Wear, *ASTM Int*, 2018, **5**, p 1–10. <https://doi.org/10.1520/G0133-05R16>
17. G. Lacob, V.G. Ghica, M. Buzatu et al., Studies on Wear Rate and Micro-Hardness of the Al/Al₂O₃/Gr Hybrid Composites Produced via Powder Metallurgy, *Compos. B Eng.*, 2015, **69**, p 603–611.
18. P. Shanmugaselvam, S. Sivaraj and P. Subash, Investigating the Wear and Hardness of Aluminium LM25 Alloy Reinforced With Nano Al₂O₃ and Nano TiB₂, *Mater. Today: Proc.*, 2019, **16**, p 1130–1136.
19. A. Pimpinelli and J. Villain, *Physics of Crystal Growth*, Cambridge University Press, Cambridge, 1998
20. W.A. Tiller, *The Science of Crystallization: Macroscopic Phenomena and Defect Generation*, Cambridge University Press, Cambridge, 1991
21. W. Kurz, D.J. Fisher, *Fundamental of Solidification*, Trans Tech Publications, Switzerland-Germany-UK-USA, 1986 (Erstauflage 1984), 242 Seiten, zahlreiche Abbildungen und Tabellen, Sachwortindex, SFr 54.00, ISBN 0-87849-523-3
22. S. Nagarjuna and D.S. Sarma, On the Variation of Lattice Parameter of Cu Solid Solution with Solute Content in Cu-Ti alloys, *Scr. Mater.*, 1999, **41**, p 359–363.
23. M.A. Meyers and K.K. Chawla, *Mechanical Behavior of Materials*, Cambridge University Press, Cambridge, 2009
24. C.P. Blankenship, E. Hornbogen and E.A. Starke, Predicting Slip Behavior in Alloys Containing Shearable and Strong Particles, *Mater. Sci. Eng. A*, 1993, **169**, p 33–41. [https://doi.org/10.1016/0921-5093\(93\)90596-7](https://doi.org/10.1016/0921-5093(93)90596-7)

25. B.Q. Li and F.E. Wawner, Dislocation Interaction with Semicoherent Precipitates (Ω Phase) in Deformed Al-Cu-Mg-Ag Alloy, *Acta Mater.*, 1998, **46**(15), p 5483–5490. [https://doi.org/10.1016/S1359-6454\(98\)00188-8](https://doi.org/10.1016/S1359-6454(98)00188-8)
26. R. Mishnev, I. Shakhova, A. Belyakov and R. Kaibyshev, Deformation Microstructures, Strengthening Mechanisms, and Electrical Conductivity in a Cu-Cr-Zr Alloy, *Mater. Sci. Eng. A*, 2015, **629**, p 29–40. <https://doi.org/10.1016/j.msea.2015.01.065>
27. M.R. Ahmadi, E. Povoden-Karadeniz, L. Whitmore, M. Stockinger, A. Falahati and E. Kozeschnik, Yield Strength Prediction in Ni-Base Alloy 718Plus Based on Thermo-Kinetic Precipitation Simulation, *Mater. Sci. Eng. A*, 2014, **608**, p 114–122. <https://doi.org/10.1016/j.msea.2014.04.054>
28. M.R. Ahmadi, E. Povoden-Karadeniz, K.I. Öksüz, A. Falahati and E. Kozeschnik, A Model for Precipitation Strengthening in Multi-Particle Systems, *Comput. Mater. Sci.*, 2014, **91**, p 173–186. <https://doi.org/10.1016/j.commatsci.2014.04.025>
29. W.B. Pearson, *A Handbook of Lattice Spacings and Structures of Metals and Alloys*, Pergamon Press, Oxford, 1964, p 531
30. Q. Lei, Z. Xiao, Hu. Weiping, B. Derby and Z. Li, Phase Transformation Behaviors and Properties of a High Strength Cu-Ni-Si Alloy, *Mater. Sci. Eng. A*, 2017, **697**, p 37–47. <https://doi.org/10.1016/j.msea.2017.05.001>
31. R. Maldonado and E. Nembach, The Formation of Precipitate Free Zones and the Growth of Grain Boundary Carbides in the Nickel-Base Superalloy NIMONIC PE16, *Acta Mater.*, 1997, **45**(1), p 213–224.
32. G. Purcek, H. Yanar, M. Demirtas, D.V. Shangina, N.R. Bochvar and S.V. Dobotkin, Microstructural, Mechanical and Tribological Properties of Ultrafine-Grained Cu-Cr-Zr Alloy Processed by High Pressure Torsion, *J. Alloy. Compd.*, 2020, **816**, p 152675. <https://doi.org/10.1016/j.jallcom.2019.152675>
33. B. Raecisnia, W.J. Poole and D.J. Lloyd, Examination of Precipitation in the Aluminum Alloy AA6111 Using Electrical Resistivity Measurements, *Mater. Sci. Eng. A*, 2006, **420**, p 245–249. <https://doi.org/10.1016/j.msea.2006.01.042S>
34. S. Chen, *Physical Property of Material*, Shanghai Jiaotong University Press, Shanghai, 1999

Publisher's Note Springer Nature remains neutral with regard to jurisdictional claims in published maps and institutional affiliations.